ORIGINAL ARTICLE

FARS1-related disorders caused by bi-allelic mutations in cytosolic phenylalanyl-tRNA synthetase genes: Look beyond the lungs!

Luise A. Schuch[1,2] | Maria Forstner[1,2] | Christina K. Rapp[1,2] | Yang Li[1,2] | Desiree E. C. Smith[3,4] | Marisa I. Mendes[3,4] | Florent Delhommel[5,6] | Michael Sattler[5,6] | Nagehan Emiralioğlu[7] | Ekim Z. Taskiran[8] | Diclehan Orhan[9] | Nural Kiper[7] | Meino Rohlfs[1] | Tim Jeske[1] | Maximilian Hastreiter[1] | Michael Gerstlauer[10] | Alba Torrent-Vernetta[11,12] | Antonio Moreno-Galdó[11,12] | Birgit Kammer[13] | Frank Brasch[14] | Simone Reu-Hofer[15] | Matthias Griese[1,2]

[1]Department of Pediatrics, Dr. von Hauner Children's Hospital, LMU Munich, Munich, Germany

[2]German Center for Lung Research (DZL), Munich, Germany

[3]Metabolic Unit, Department of Clinical Chemistry, Amsterdam UMC, Vrije Universiteit Amsterdam, Amsterdam, The Netherlands

[4]Amsterdam Gastroenterology & Metabolism, Amsterdam Neuroscience, Amsterdam, The Netherlands

[5]Institute of Structural Biology, Helmholtz Zentrum München, Neuherberg, Germany

[6]Center for Integrated Protein Science Munich, Department of Chemistry, Technical University of Munich, Garching, Germany

[7]Department of Pediatric Pulmonology, Faculty of Medicine, Hacettepe University, Ankara, Turkey

[8]Department of Medical Genetics, Faculty of Medicine, Hacettepe University, Ankara, Turkey

[9]Department of Pediatric Pathology, Faculty of Medicine, Hacettepe University, Ankara, Turkey

[10]Children's Hospital Augsburg, Augsburg University, Augsburg, Germany

[11]Pediatric Allergy and Pulmonology Section, Department of Pediatrics, Vall d'Hebron Hospital Universitari, Vall d'Hebron Barcelona Hospital Campus, Universitat Autònoma de Barcelona, Barcelona, Spain

[12]Center for Biomedical Research on Rare Diseases (CIBERER), Instituto de Salud Carlos III, Madrid, Spain

[13]Pediatric Radiology, Clinic for Radiology, LMU Munich, Munich, Germany

[14]Institute for Pathology, Klinikum Bielefeld Mitte, Bielefeld, Germany

[15]Department of Pathology, Würzburg University, Würzburg, Germany

Correspondence
Matthias Griese, Department of Pediatrics, Dr. von Hauner Children's Hospital, LMU Munich, Lindwurmstraße 4, D-80337 Munich, Germany.
Email: matthias.griese@med.uni-muenchen.de

Funding information
Deutsche Forschungsgemeinschaft, Grant/Award Number: Gr 970/9-1; Deutsches

Abstract

Aminoacyl-tRNA synthetases (ARSs) catalyze the first step of protein biosynthesis (canonical function) and have additional (non-canonical) functions outside of translation. Bi-allelic pathogenic variants in genes encoding ARSs are associated with various recessive mitochondrial and multisystem disorders. We describe here a multisystem clinical phenotype based on bi-allelic mutations in the two genes (*FARSA*, *FARSB*) encoding distinct subunits for tetrameric

Luise A. Schuch and Maria Forstner shared first authorship.

cytosolic phenylalanyl-tRNA synthetase (FARS1). Interstitial lung disease with cholesterol pneumonitis on histology emerged as an early characteristic feature and significantly determined disease burden. Additional clinical characteristics of the patients included neurological findings, liver dysfunction, and connective tissue, muscular and vascular abnormalities. Structural modeling of newly identified missense mutations in the alpha subunit of FARS1, *FARSA*, showed exclusive mapping to the enzyme's conserved catalytic domain. Patient-derived mutant cells displayed compromised aminoacylation activity in two cases, while remaining unaffected in another. Collectively, these findings expand current knowledge about the human ARS disease spectrum and support a loss of canonical and non-canonical function in FARS1-associated recessive disease.

KEYWORDS
aminoacyl-tRNA synthetases, cholesterol pneumonitis, FARS1, *FARSA*, *FARSB*, children´s interstitial lung disease (chILD) lipoid pneumonia

1 | INTRODUCTION

Aminoacyl-tRNA synthetases (ARSs) are ubiquitous enzymes that fulfill an essential role in protein biosynthesis by covalently linking a tRNA molecule to its cognate amino acid. In addition, ARSs have key functions in various cellular pathways outside of translation.[1-3] In humans, two subsets of ARSs can be distinguished based on their cytoplasmic or mitochondrial localization. With rare exception, separate genes, unique for each amino acid, encode for both cytoplasmic and mitochondrial ARSs. More than 60 disorders are associated with mutations in ARS genes and, depending on their individual genotype, follow both dominant or recessive inheritance patterns.[4-10]

Cytosolic phenylalanyl-tRNA synthetase (FARS1) ranks among the most complex of the ARSs with a hetero-tetrameric structure, consisting of two FARS alpha (FARSA) and two FARS beta (FARSB) subunits.[11] The hypothesis that both genes may be associated with a similar multisystemic human disease, including features of interstitial lung disease, liver disease, neurological manifestations, and growth restriction (MIM: 619013, 613 658), needs further support. Whereas 11 individuals presenting with bi-allelic mutations in *FARSB* are described,[9,12,13] information on *FARSA*-related disease is rare and comes from a single case report describing a patient with mutations in *FARSA* and features of interstitial lung disease, cerebral and skeletal abnormalities, hypotonia, and liver dysfunction.[10]

Here, we report three unrelated individuals with identified bi-allelic variants in *FARSA* (MIM: 602918), and two unrelated individuals presenting bi-allelic variants in the gene encoding the beta subunit, *FARSB* (MIM: 609690). We provide biochemical and functional proof of novel genetic variants, spotlight the value of rare but indicative interstitial lung disease as a clue for diagnosis, give details on the long-term clinical course including treatment and outcome, and review the spectrum of FARS1-associated recessive disease.

2 | MATERIAL AND METHODS

Patients were recruited from the European Management Platform for Interstitial Lung Disease (chILD-EU) registry by searching the database for children with chronic interstitial lung disease of unknown cause, and in-depth analysis of *ARS* genes by whole exome sequencing (WES) was performed. Six subjects with predicted disease-causing variants in *FARSA* and *FARSB* were retrieved, one was published independently.[10] Patients and families gave their written informed consent to participate in the chILD-EU consultation and diagnosis program. All human subject research was in accordance with current ethical standards and approved by the Ethics Committee of the University of Munich, Germany (EK 111–13, EK 20–329).

2.1 | Whole exome sequencing and variant prioritization

Genomic DNA was isolated from whole blood using the QIAmp DNA Mini Kit (Qiagen, Hilden, Germany) according to the manufacturer's instructions. Exonic regions were enriched with SureSelectXT Human All Exon V6 + UTR kit (Agilent, Santa Clara, CA) and sequenced as 150 bp paired-end runs on an Illumina NextSeq500 (ILLUMINA, San Diego, CA). Reads were aligned to the human reference genome GRCh37 by Burrows-Wheeler Aligner (v.0.7.15).[14] Genome Analysis Tool Kit (GATK v3.8)[15] software was used to analyze the data. Functional annotation was added using Variant Effect Predictor (VEP), Ensembl release 95.[16] Rare variants (MAF < 1%) were filtered using an in-house SQL database incorporating frequency information from the 1000 Genomes Project[17] and gnomAD.[18] Filtered variants were evaluated based on predicted pathogenicity scores and an autosomal recessive inheritance pattern including homozygous and compound heterozygous variant pairs identified by Smart-Phase.[19] All patients were analyzed as trios; variants that remained after filtering are presented in Table S2. Sanger sequencing was used to confirm the identified mutations in *FARSA* and *FARSB* and to determine the carrier status of parents

and the unaffected sibling in family 1 (for primers, see supplementary information S1).

2.2 | Histopathology, isolation of patient-derived cell lines and cell culture

Tissue for diagnosis was obtained by open lung biopsy. Following formalin fixation and paraffin embedding, slides were stained with Hematoxylin–Eosin (HE), Elastica van Gieson (EvG), Prussian Blue, and Periodic Acid-Schiff (PAS). All readings were made by a pathologist specialized in pediatric interstitial lung disease.

Fibroblasts were obtained from skin punch biopsy of affected individuals and cultured in Dulbecco's Modified Eagle Medium/F12 (DMEM) (Pan Biotech, Aidenbach, Germany) supplemented with 10% FBS (Sigma-Aldrich, St. Louis, MO) (vol/vol), and 1% Antibiotic-Antimycotic (Thermo Fisher, Waltham, MA) (vol/vol) at 37°C and 5% CO_2. Cells were regularly split after reaching confluency of 80%–90%.

PBMCs were isolated from whole blood samples by density gradient centrifugation with Biocoll (Merck, Darmstadt, Germany) and subsequently incubated with B95-8 cell supernatants (Leibniz Institute, DSMZ, Germany) and 0.01% cyclosporine A (Sigma-Aldrich) (wt/vol) to give rise to Epstein–Barr Virus Immortalized Lymphoblastoid Cell Lines (EBV-LCLs). Cells were maintained in RPMI 1640 medium with GlutaMAX™ (Thermo Fisher), supplemented with 10% FBS (Sigma-Aldrich) (vol/vol), 10 mM HEPES (Thermo Fisher), and 1% Antibiotic-Antimycotic (Thermo Fisher) (vol/vol) at 37°C and 5% CO_2.

2.3 | Modeling of the human FARS1-tRNA^{Phe} complex structure

The structure of the *Thermus thermophilus* tRNA^{Phe} molecule (PDB: 2IY5)[20] was aligned with the crystal structure of human FARS1 (PDB: 3L4G)[21] using PyMOL[22] to model the position of tRNA^{Phe} and the phenylalanyl-adenylate.

2.4 | Conservation analysis of FARSA amino acid residues

Conservation analysis was performed with ConSurf Server.[23] Initial sequence selection was performed on the Uniref90 database using an E-value threshold of 0.0001. Within this pool, the best 70 FARSA sequences were manually selected. Final alignment was performed with the MAFFT-L-INS-i method and scoring was calculated using the Bayesian method.

2.5 | RNA isolation and quantitative reverse transcription PCR

Total RNA was isolated from cultured cells using the High Pure RNA Isolation Kit (Roche, Basel, Switzerland). RNA yield and purity were measured on a NanoDrop spectrophotometer (NanoDrop Technologies, Thermo Fisher). 1 μg of RNA was subsequently reverse transcribed with the Tetro cDNA Synthesis Kit (Bioline, Meridian Bioscience, Cincinnati, OH). Real-Time PCR was performed in a thermal cycler (StepOnePlus, Applied Biosystems, Thermo Fisher) with SensiFast SYBR Hi-ROX reagent (Bioline) capturing target genes *FARSA*, *FARSB*, and the ribosomal internal control gene *RPS29* (primers, see supplementary information S1). Fold change of target gene expression was calculated based on the comparative C_T method.[24]

2.6 | Western blot and densitometry

Cells were lysed in radioimmunoprecipitation assay buffer (0.15 M sodium chloride, 1% Triton X100 [vol/vol], 0.5% sodium deoxycholate [Sigma-Aldrich] [wt/vol], 5 mM ethylenediaminetetraacetic acid [GE Healthcare, Chicago, IL], 50 mM Tris [pH = 8] [Merck]). 20 μg of protein were subjected to polyacrylamide- gel electrophoresis on a NuPage Mini 3%–8% Tris-Acetate gel (Thermo Fisher) and blotted to a polyvinylidene fluoride membrane (Merck). Antigen targets were detected using the rabbit polyclonal primary antibodies anti-FARSA 18121-1-AP (Proteintech, St. Leon-Rot, Germany), and anti-FARSB HPA036677 (Sigma-Aldrich), followed by incubation with HRP-conjugated goat anti- rabbit IgG (H + L) secondary antibody (Thermo Fisher). B–actin quantification (sc-47 778 HRP, Santa Cruz, Dallas, TX) served as a loading control. Proteins were detected using SuperSignal West Femto Maximum Sensitivity Substrate (Thermo Fisher). Relative band intensities were analyzed using the Image J software.[25]

2.7 | Aminoacylation assay

FARS1 activity was assessed by steady-state aminoacylation assays in cells of patients and family members. Cytosolic fractions of lysates were incubated at 37°C with 0.3 mM [D_5]-phenylalanine and [D_2]-tyrosine (Cambridge Isotope Laboratories, Tewksbury, MA) in a 50 mM Tris buffer, pH 7.5, containing 1 mM ATP, 0.2 mM yeast total tRNA, 1 mg/ml bovine albumin serum, 12 mM $MgCl$, 25 mM KCl and 1 mM dithiothreitol (all Sigma-Aldrich). [^{13}C]-phenylalanine and [$^{13}C_9$]-tyrosine (Cambridge Isotope Laboratories) were added as internal standards. Labeled amino acids were quantified by liquid chromatography–tandem mass spectrometry. Intra-assay variation was <15%. For kinetic studies, K_m and V_{max} values for phenylalanine and tyrosine were calculated by measuring six different concentrations in the range of 0.009–0.6 mmol/L. Data were subsequently analyzed using Graph Pad Prism 8.2.1 (GraphPad Software, La Jolla, CA).

3 | RESULTS

3.1 | Clinical characteristics of patients with newly identified *FARSA/FARSB* variants

All five unrelated patients (P1, P2, P3, P16, P17) with novel bi-allelic variants in *FARSA* or *FARSB* (Figure 1) were identified clinically due to
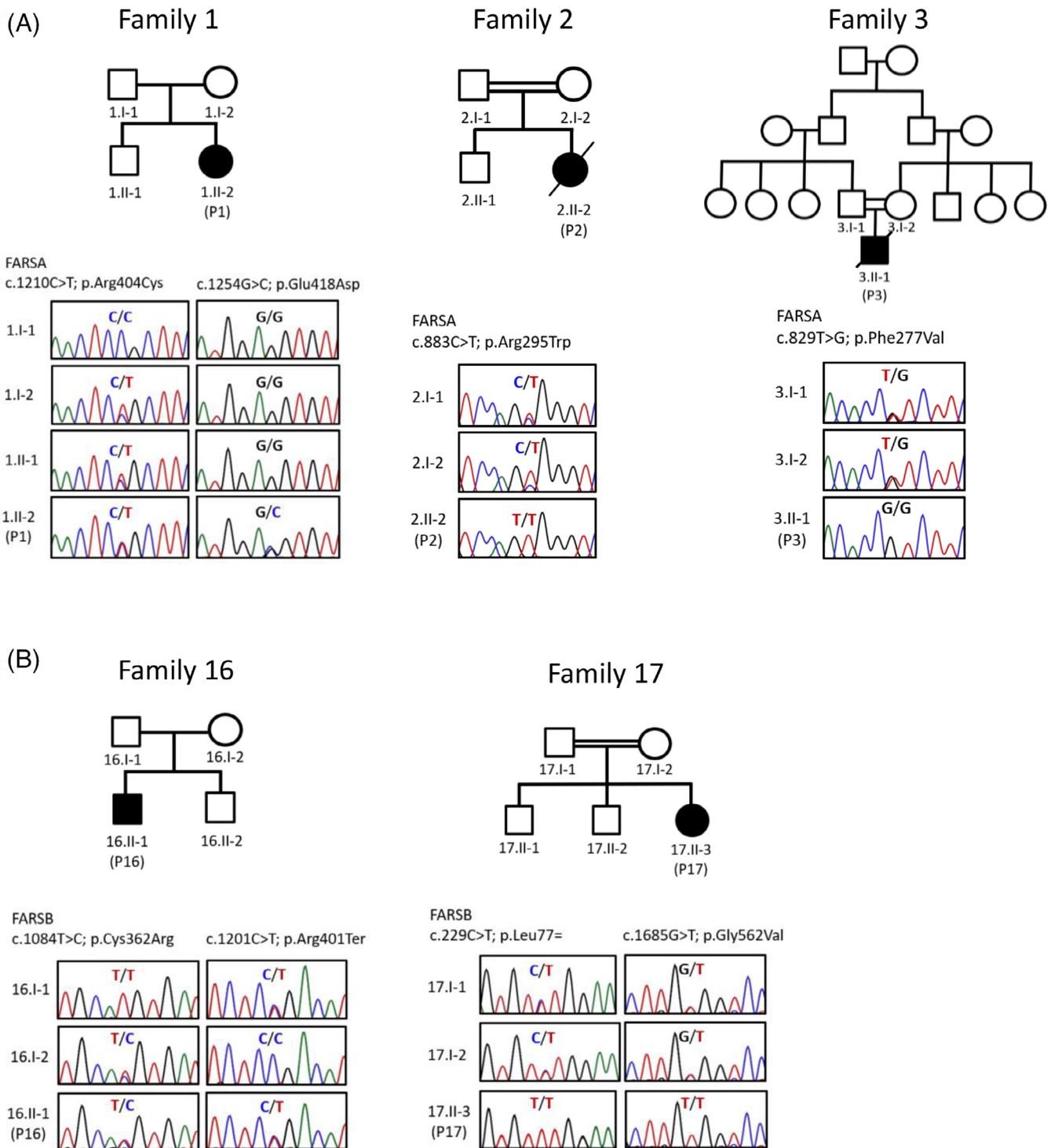
FIGURE 1 Family pedigrees with segregation of newly identified variants in *FARSA* (NM_004461.3, NP_004452.1) (A) or *FARSB* (NM_005687.5, NP_005678.3) (B) confirmed by Sanger sequencing. Predicted effects on cDNA and protein for affected and unaffected individuals are indicated. Patients are marked P1-P3 (*FARSA*) and P16, P17 (*FARSB*). For families 2, 3, and 17, consanguinity of the unaffected parents was reported [Colour figure can be viewed at wileyonlinelibrary.com]

their prominent and distinct pulmonary phenotype. Common to all was a peculiar chronic interstitial lung disease starting early in life and characterized by bilateral ground-glass opacification on HR-CT, and cholesterol pneumonitis in lung histology. Additional abnormalities in

other organ systems were summarized, suggesting a multi-organ disorder (Figure 4, Table S1).

Patient 1 was born hypotonic with hyperflexible joints, had arachnoid fingers and delayed motor development. At the age of 5 years,
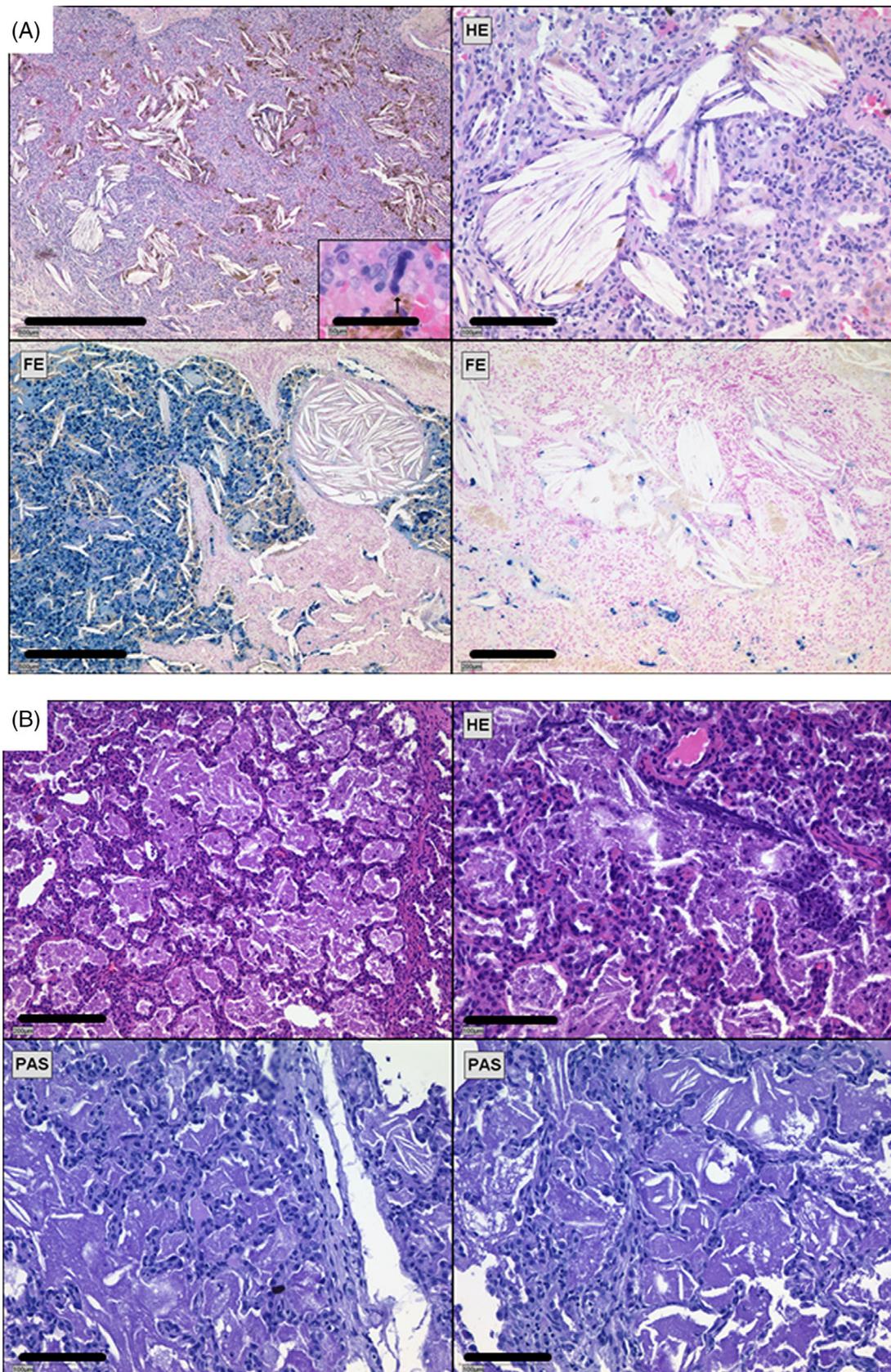
FIGURE 2 Histopathology of the lungs. (A) Prominent cholesterol pneumonia with intra-alveolar and interstitial cholesterol granulomas. Note combination with fresh and older bleeding with accumulation of iron-storing macrophages, and megakaryocyte emboli resulting from pulmonary hypertension (insert arrow) (P1, age of 8.6 years; hematoxylin–eosin (HE) staining; in upper left panel, scale bar 500 μm; insert, scale bar 50 μm, and upper right panel, scale bar 100 μm; iron (Prussian Blue, FE) staining in lower left panel and lower right panel, scale bar 500 and 200 μm). (B) Pulmonary alveolar proteinosis with dense intra-alveolar accumulation of Periodic acid–Schiff (PAS)-positive granules and cholesterol clefts (P2, age of 8 months; HE-staining in upper panels, scale bar 200 μm (left) and 100 μm (right), PAS-staining in lower panels, scale bars 100 μm) [Colour figure can be viewed at wileyonlinelibrary.com]
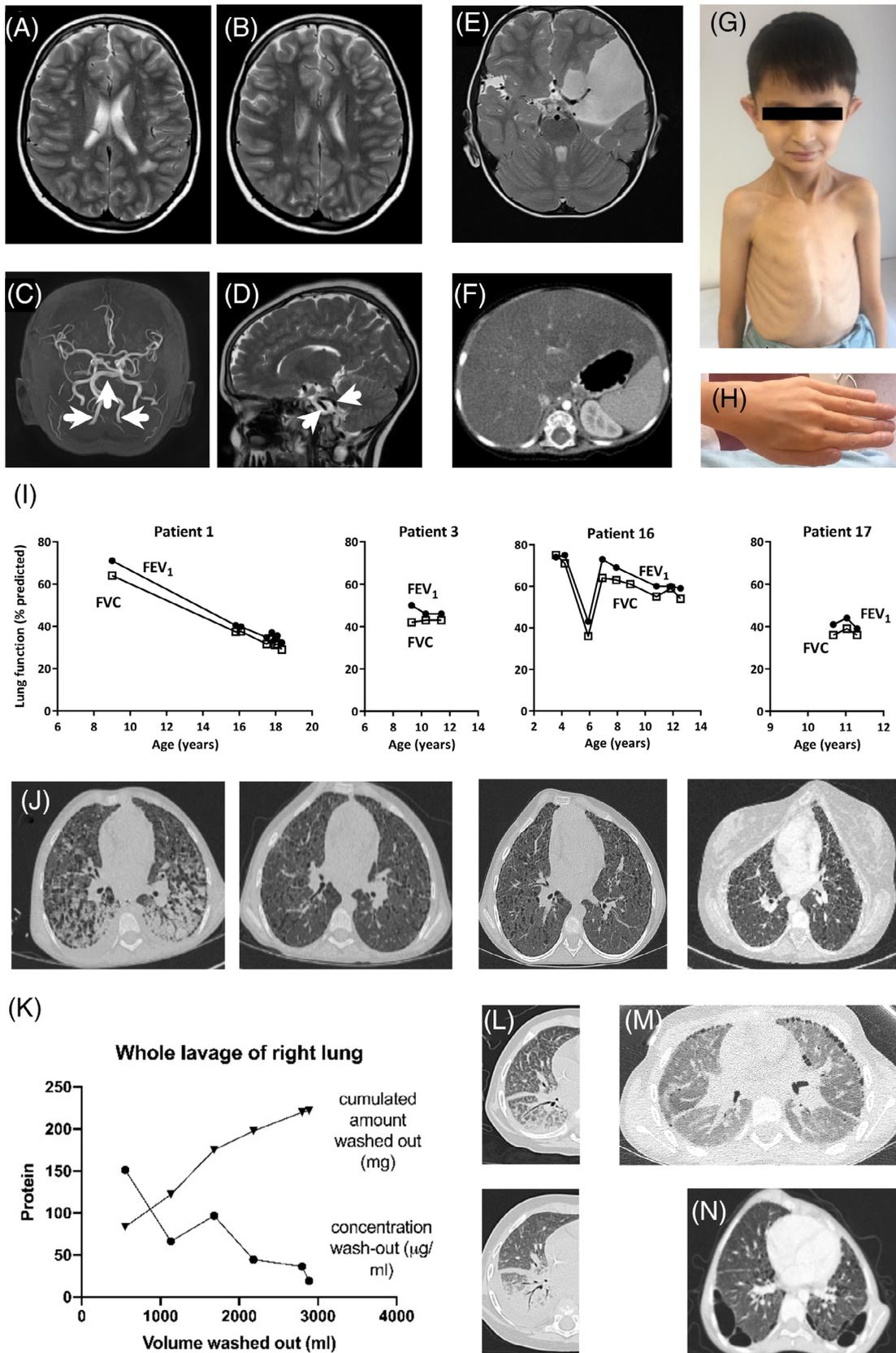
FIGURE 3 Legend on next page.

growth hormone resistance (Laron-type, no molecular confirmation) was diagnosed, and IGF-1 treatment was applied for 6 years (reaching 20th percentile for height). Her brain MRIs at the age of 8.8 and 9.5 years demonstrated multiple unspecific white matter lesions in a predominantly subcortical location, increased in number and size at the age of 17 years. Elongated brain arteries were noted (Figure 3(A–D)). She had hepatosplenomegaly and abdominal ultrasound revealed steatosis of the liver. At the age of 8.4 years, she presented with a protracted respiratory tract infection, was severely hypoxemic on admission, and needed intubation and ventilation for 2 weeks. Bilateral clubbing was noted. Cardiac echo (at age 8.7 years) gave slightly elevated pulmonary artery pressures, and 7 years later, there was no evidence for pulmonary hypertension. After recovery, she had a forced vital capacity of 73% of predicted, oxygen saturation during sleep between 88% and 91%, and normal pCO_2. Her chest X-ray showed bilateral ground-glass and reticular opacities. Chest CT initially showed patchy consolidations which resolved over time, whereas fibrosing lung disease became more prominent (Figure 3(J)). Lung biopsy demonstrated intra-alveolar and interstitial cholesterol granulomas, in combination with pulmonary hemorrhage at the age of 8.6 years, consistent with cholesterol pneumonia (Figure 2(A)). The course of lung disease was progressive (Figure 3(I)) despite various treatments, including a protein-rich diet and phenylalanine substitution. Currently she is stable at low lung function and evaluated for lung transplantation.

Patient 2 was referred at 1 month of age for failure to thrive, vomiting, chronic loose stools without pancreatic insufficiency, hyperphosphaturia, and osteopenia. An initial examination revealed hepatosplenomegaly, also on CT (Figure 3(F)), with hypoalbuminemia, increased neutral lipid storage in hepatocytes, and signs of focal fibrosis and cholestasis in liver biopsy. On physical examination, she had visible and palpable subcutaneous fat pads on her forearms and around her knees. She had hypotonic muscle tone, intermittent nystagmus, and a global neurodevelopmental delay. Brain ultrasound was normal. The infant was tachypneic since 5 months of age and suffered from recurrent respiratory infections up to the age of 1 year. Initial and consecutive chest X-rays showed bilateral homogenous ground-glass opacities, bronchial wall thickening and generalized overinflation,

and chest CTs revealed interlobular septal thickening and crazy-paving pattern, increasing over time, despite therapeutic lung lavage (Figure 3(L)). Lung biopsy confirmed pulmonary alveolar proteinosis with intra-alveolar and intraseptal cholesterol crystals (Figure 2(B)). Over time respiratory distress increased. A therapeutic lavage removed 62 g of protein from the right lung, however, the infant died of respiratory failure at the age of 1.3 years.

Patient 3 was referred at the age of 5 years for recurrent lower airway infections and chronic cough for more than 3 months. He had growth retardation, pectus carinatum, digital clubbing, and a sensorineural hearing defect (Figure 3(G,H)). A CT scan at the age of 7.5 years demonstrated ground-glass opacification and reticulation, bilateral emphysema, bullae, nodules, focal consolidations, emphysema, and air trapping on expiration (Figure 3(N)). Lung biopsy showed hyperinflated and emphysematous airspaces with an increased infiltration of inflammatory cells and cholesterol pneumonia. In addition, growth hormone deficiency was detected, and cranial MRI revealed an arachnoid cyst (Figure 3(E)), but he presented neurologically normal. Despite various treatments, his clinical status deteriorated gradually with increasing hypoxemia, dyspnea, pronounced pectus carinatum, slightly altered liver enzyme values, and failure to thrive. After a several months period of increasing respiratory distress, he died of respiratory failure at the age of 12.9 years.

Patient 16 suffered from a mild bronchiolitis at the age of 2 months and a self-limiting bronchitis at the age of 7 months. At the age of 2 years, digital clubbing was observed on an emergency visit for gastroenteritis. He was asymptomatic with normal oxygen saturation on room air, however, chest X-ray and CT scan revealed diffuse ground-glass opacities, septal thickening, and subpleural cysts (Figure 3(M)). Lung tissue showed cholesterol granulomas and clefts, pneumocyte hyperplasia, and mild fibrous septal thickening. Due to chronic moderate headaches, brain MRI was performed at the age of 8 years and revealed bilateral focal and non-confluent glioticdemyelinating lesions with dilated perivascular spaces. At the age of 10 years, he was diagnosed with sensorineural hearing loss. Otherwise, neurological examination was unremarkable. An abdominal ultrasound revealed mildly diffuse hyperechoic liver parenchyma and renal asymmetry with a smaller right kidney. Currently at the age of

FIGURE 3 (A,B) Cranial MRI, axial T2-w images (P1, age 17 years) with multiple non-specific white matter lesions in a predominantly subcortical location, which may indicate cerebral small vessel disease. MR-Angio (C) and T2-w sagittal image (D) show an unusual elongation of both vertebral arteries and the basal artery as well as of all arteries of the circle of Willis (arrows). No aneurysms present. (E) T2-w cranial MRI with large arachnoid cyst (P3, age 5 years). (F) Liver enlargement in CT with hypodense liver parenchyma likely representing fatty liver (P2, age 10 months). (G,H) Images of P3 highlighting pectus carinatum, failure to thrive, and digital clubbing (age 12 years). (I) Restrictive lung disease in early childhood with rapid progression. FEV_1, forced expiratory volume in 1 s, FVC, forced vital capacity. (J) Chest CT (P1, 8.4 years) (first left) with bilateral diffuse ground-glass attenuation, interstitial reticular markings, and patchy consolidations. Overtime (ages 8.8, 11, 17 years) (from left to right) development of many small periseptal and subpleural cysts, diffuse ground-glass opacities, and pronounced pectus carinatum, loss of volume, architectural distortion. (K) Therapeutic bronchoalveolar lavage of the right lung (P7, age 5 years). Protein wash-out with six lavage cycles. (L) Axial HR-CT (only right side shown) before (upper panel) and 1 day after (lower panel) therapeutic lavage of the middle lobe with almost complete clearance of the diffuse ground-glass opacification and interlobular septal thickening in concert with increasing pleural effusion and dependent consolidation in the lower lobe (P2, age 10 months). (M) Chest CT with diffuse ground-glass opacities and numerous subpleural cysts (P16, age 8 years). (N) Chest CT with characteristic pectus carinatum chest deformity and differently shaped subpleural bullae and emphysematous changes, pleural thickening, multiple intraparenchymal lung cysts, and bilateral hilar lymphadenopathies (P3, age 7.5 years) [Colour figure can be viewed at wileyonlinelibrary.com]

13 years, he presents with persistent failure to thrive. He follows a protein-rich diet that he was recommended to adhere to. On physical examination, lung auscultation and resting oxygen saturation are normal, but he still shows prominent digital clubbing. Lung function tests show a reduced spirometry and diffusing capacity for CO (58% of predicted) (Figure 3(I)).

Patient 17 was referred at the age of 8 years for failure to thrive and chronic cough and dyspnea, persistent for 1 year. On physical examination, she presented with pectus excavatum and digital clubbing. Chest X-ray showed bilateral interstitial appearance and CT scan identified diffuse ground-glass opacities and cysts, subpleurally and scattered throughout all lobes. Lung biopsy revealed cholesterol pneumonia associated with mild chronic interstitial inflammation and fibrosis, foam cell aggregates, mild lymphoid hyperplasia without lymphoid follicles, and mild chronic pleuritis with fat metaplasia. She has a history of chronic diarrhea from the age of 3 months, which improved over time with a specific formula of nutrition. Due to proteinuria and hypoalbuminemia, further nephrological and metabolic diagnostics were performed; however, no other abnormalities were detected. An abdominal ultrasound was normal. Currently at the age of 12 years, she has reduced resting oxygen saturation around 90% and is on long-term oxygen supplementation.

3.2 | Bi-allelic variants in *FARSA* and *FARSB* cause FARS1-related disorders

Review of the clinical features of the five unrelated patients with novel bi-allelic variants in *FARSA* or *FARSB* and previously published cases described a complex phenotype, manifesting during early childhood, after an uneventful neonatal period (Figure 4). Besides the common distinct pulmonary phenotype and failure to thrive, abnormal neuromuscular features occurred in more than two thirds of the patients. About half of the subjects had abdominal and hepatic abnormalities. Less frequent findings in multiple other organ systems were present at similar prevalence, independent of the underlying FARS1 subunit affected.

Exome sequencing identified compound heterozygous *FARSA* variants c.(1210C > T), p.(R404C) and c.(1254G > C), p.(E418D) (*de novo*) in patient 1 and homozygous variants (c.883 C > T), p.(R295W) and c.(829 T > G), p.(F277V) in patient 2 and 3, both with consanguineous family background. Compound heterozygous *FARSB* variants c.(1084 T > C), p.(C362R) and c.(1201C > T), p.(R401*) were identified in patient 16 and homozygous variants c.(229C > T), p.(L77=) and c.(1685G > T), p.(G562V) in patient 17 with consanguineous family background. Variants were annotated on NM_004461.3 (NP_004452.1) and NM_005687.5 (NP_005678.3), respectively (Figure 1).

3.3 | *FARSA* variant effect prediction on protein structure

With the exception of patient 2 (R295W, average conservation), the presented variants in *FARSA* were strictly conserved (Figure S1) and

absent or extremely rare in gnomAD (Table S1A). Structurally, the FARSA protein consists of two main regions. The N-terminal site contains three subdomains with characteristic helix-turn-helix structures, forming a DNA/dsRNA binding domain (DBD1/2/3) and likely functioning to recognize and bind tRNA[Phe]. The DBD-domain connects through a linker region to the C-terminal catalytic domain with subdomains A1/A2 which participate in tRNA binding and aminoacylation.[21,26] All identified variants were located exclusively in the A1/A2 domain (Figure 5(A)).

To investigate the impact of both these and previously reported variants[10] on FARS1 structure and function, we aligned *T. thermophilus* tRNA[Phe] (PDB: 2IY5) with the crystal structure of human FARS1 (PDB: 3L4G) (Figure 5(B)). In this model, three residues affected by the missense mutations potentially interfere directly with the catalytic activity, due to their proximity to the active site: E418D, N410K, and F256L. The first, E418, interacts with conserved residues K406, E431, and N434 and is located close to the 3′ end of the tRNA, where phenylalanine is loaded. The substitution by aspartate incorporates a shorter side chain that might interfere with this hydrogen network and either affects tRNA binding or the transfer of the amino acid from its binding site to the tRNA (Figure 5(Ci)). The second, N410, forms two hydrogen bonds with the conserved residue N434. These bonds have previously been predicted to influence rigidity of the phenylalanine binding site[21] and the substitution by lysine at this position will very likely modify the conformation of the active site (Figure 5(Cii)). The third, F256, is an absolutely conserved residue in a very well conserved region (amino acids 253–278). Structurally, it is located at the back of the active site in a hydrophobic pocket **composed** of aromatic and hydrophobic residues (W257, P289, Y292, V293, A261, A319). The substitution by leucine conserves the hydrophobic nature of the residue, albeit to a lesser extent, and might slightly destabilize the pocket, thus affecting the active site (Figure 5(Ciii)).

The other variants F277V, R404C, and R295W primarily affect residues close to interfaces between subunits A/B and might interfere with the overall structure of the FARS1 complex. Residue F277 is located at a strong hydrophobic pocket at the interface between subunits and is composed of strictly conserved residues on both subunit sides. Based on the aligned homologous structures, it is also in close proximity with the tRNA. Given the strict conservation of the interface, it is likely that functional FARSA/B is destabilized by the substitution, thus likely affecting its enzymatic activity (Figure 5(Civ)). R404 is a well conserved residue (98%) close to the active site, but it is also located near an interface with FARSB and likely forms hydrogen bonds with E26 from FARSB and the strictly conserved W429 from FARSA. A substitution by cysteine (R404C) would impact this hydrogen bond network and might impact the interactions between subunits. Alternatively, the substitution might induce conformational changes down into the proximal active site (12.3 Å), thus directly affecting the activity (Figure 5(Cv)). The last residue, R295, is solvent exposed and located in a variable region of the protein. R295 is partially conserved (87% in our alignment) but can be substituted by other residues containing NH_2 groups: lysine (11%) and asparagine

Subject		FARSA	FARSB	Σ	%
Respiratory system	interstitial lung disease			17/17	100
	cholesterol pneumonitis			11/11	100
	pulmonary alveolar proteinosis			2/11	18
	cystic lung disease			10/17	59
	digital clubbing			7/17	41
Skeletal system	pectus carinatum/excavatum			6/17	35
	joint hyperflexibility			6/17	35
	osteopenia			5/17	29
	Marfan-like syndrome (arachnodactyly, body)			4/17	24
Musculature	hypotonia			9/17	53
	decreased muscle mass			9/17	53
	abnormal muscle histology/respiratory chain function			6/6	100
Nervous system	neurodevelopmental/motor/speech delay			10/17	59
	headache/migraine			2/17	12
	seizures			2/17	12
	extrapyramidal symptoms			1/17	6
	microcephaly			7/17	41
	brain cysts			2/15	13
	brain calcifications			9/15	60
	white matter/gliotic-demyelinating lesions			2/15	13
	brain aneurysm/elongated arteries			3/15	20
	brain hemorrhage			2/15	13
	hypopituitarism			1/15	7
	hydrocephalus			2/17	12
Liver, nutrition	feeding difficulties/emesis/diarrhea/chronic gastritis			7/17	41
	hepatomegaly/hepatosplenomegaly			6/17	35
	abnormal liver values (blood)			7/17	41
	liver steatosis/ fibrosis/ cirrhosis/ hyperechogenicity			8/8	100
Cardiovascular system	structural heart/vessel defects			5/17	29
	arterial hypertension			2/17	12
Immune system	IgG2 deficiency			1/17	6
Urinary system	vesicoureteral reflux			2/17	12
	proteinuria			3/17	18
	renal artery stenosis			1/17	6
	hyperphosphaturia			1/17	6
	glomerulosclerosis			1/1	100
	nephrolithiasis			1/17	6
	renal asymmetry			1/17	6
	renal hyperechogenicity			1/17	6
Eye	abnormal eye movement			2/17	12
Ear	sensorineural hearing impairment			2/17	12
Growth	failure to thrive			16/17	94
Endocrine system	hypothyroidism			1/17	6
Blood and blood-forming system	abnormal blood cell counts			4/17	24
Metabolism/homeostasis	hypoalbuminemia			9/17	53
	abnormal metabolite values (blood)			3/17	18
Gastrointestinal tract	hernia			3/17	18
	intestinal malrotation			2/17	12
	gastroesophageal reflux			2/17	12
	gastroesophageal varices/hemorrhage			1/17	6
Dysmorphic features	face/body appearance			13/17	76
Skin	poor wound healing			2/17	12
	anasarca			1/17	6
	abnormal subcutaneous fat tissue distribution			5/17	29

Patient columns: P1 (presented here), P2 (presented here), P3 (presented here), P4 (Krenke et al., 2019), P5 (P1 in Xu et al., 2018), P6 (P2 in Xu et al., 2018), P7 (P3 in Xu et al., 2018), P8 (P4 in Xu et al., 2018), P9 (P5 in Xu et al., 2018), P10 (Antonellis et al., 2018), P11 (IV-8 in Zadjali et al., 2018), P12 (IV-1 in Zadjali et al., 2018), P13 (IV-2 in Zadjali et al., 2018), P14 (IV-3 in Zadjali et al., 2018), P15 (IV-4 in Zadjali et al., 2018), P16 (presented here), P17 (presented here)

FIGURE 4 Summarized graphical clinical phenotype of patients with mutations in *FARSA* or *FARSB* described here (P1-P3, P16, P17) (marked in red) or in the literature (P4-P15) (marked in black, see Table S1 for details) (adapted from Ref. 4). Black and white squares reflect positivity and negativity for symptoms, gray squares reflect presence of symptoms "in most"[12] (calculation with 2/3 of individuals). Unknown status is indicated by the slash symbol [Colour figure can be viewed at wileyonlinelibrary.com]
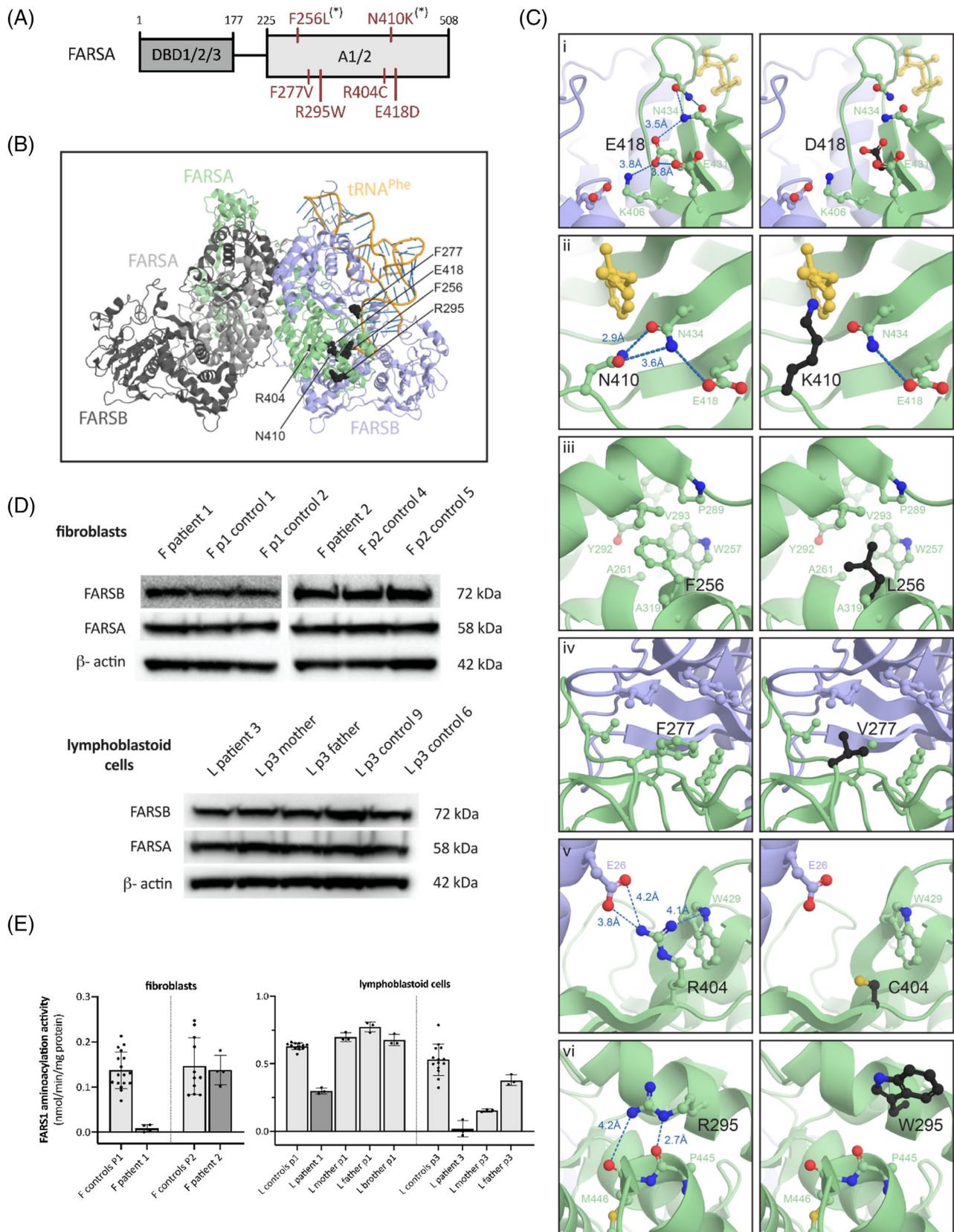
FIGURE 5 Legend on next page.

(2%) (Figure S2). The side chains likely form two hydrogen bonds with the backbone carbonyl of the residues P445 and M446. With the substitution lysine or asparagine, one of these hydrogen bonds could be conserved. However, the substitution by a tryptophan does not allow these hydrogen bonds and would potentially weaken the structural integrity of the region (Figure 5(Cvi)).

3.4 | Aminoacylation activity of FARS1 complex

To further characterize the impact of the mutations on aminoacylation, FARS1 enzyme activity levels were determined in fibroblasts or EBV-transformed lymphoblastoid cell lines (EBV-LCLs) of patients and family members (Figure 5(E)). Patient 1 (E418D/R404C) had FARS1 activity reduced to ~5% in fibroblasts and ~50% in the EBV-LCL. Enzymatic activity in carriers (R404C/WT), that is, the mother or the brother of patient 1, was normal indicating that E418D, consistent with its location near the tRNA end, mainly affects aminoacylation. In contrast, fibroblasts of patient 2 (R295W/R295W) had normal FARS1 activity level (see also Figure S2). In the EBV-LCLs of family 3 (F277V/F277V), we found FARS1 activity decreased to ~5% in the patient and ~30%–75% in heterozygous parents, suggesting that F277V reduces aminoacylation activity in a dose-dependent manner, but does not completely abolish it, reflective of its hypomorphic nature. All patients and carriers showed normal FARSA and FARSB transcript and protein expression (Figure 5(D), Figure S3(A,B,C)).

4 | DISCUSSION

The data provided here support the view that FARS1-associated recessive disease represents an ample clinical phenotype involving multiple organ systems caused by a disturbance of cytosolic phenylalanyl-tRNA synthetase. Due to the heterotetrameric structure of the FARS1 complex, consisting of two alpha and two beta subunits, we expect a common underlying pathomechanism that may be rooted in either bi-allelic variants in FARSA, the gene encoding the alpha subunit of FARS1 or its beta subunit, FARSB.

The FARS1 phenotype manifests in more than 10 organs (Figure 4) and varies in expression and severity of symptoms interindividually. It partially overlaps with the phenotype observed in other cytoplasmic ARS diseases which commonly present as a broad multisystem spectrum, typically with a neurological component.[5] A dominant and unifying feature of FARS1 cases was its uncommon but distinctive interstitial lung disease phenotype, defined by a characteristic chest CT pattern and cholesterol pneumonitis in all individuals where histology was available. The rare pulmonary phenotype should therefore be an important red flag to start systematic search for other clinical organ involvement.

The identified variants in FARSA and FARSB were rare (MAF < 1%), predicted as pathogenic, and detected in trans if compound heterozygous. The majority affect highly evolutionary conserved amino acid residues (shown for FARSA in Figure S1). Patient 16 presented a missense mutation in combination with a predicted loss of function allele. This pattern matches the typical recessive ARS disease genotype, which usually encompasses either homozygosity for missense mutations, compound heterozygosity for missense mutations or compound heterozygosity for one missense mutation and one null allele.[5]

Considering the vital role of ARS genes for protein synthesis, mutations typically present as hypomorphic rather than loss of function alleles. Accordingly, we have detected basic FARS1 activity in all our patient-derived cell lines with cells growing normally. FARS1 aminoacylation rate was compromised in two patient cell lines, whereas it was normal in another. Normal ARS activity in vitro might not necessarily reflect its activity in vivo. Alternatively, the results suggest that aminoacylation may represent a FARS1 function not pivotal for disease pathogenesis. This concept is in line with previous mechanistic studies in FARSB mutant patient-derived cells.[9] Bi-allelic FARS1 mutations likely express their pathogenicity through a yet undetermined molecular pathway where gene dose has fallen below a critical threshold. Concordantly, several publications link ARSs to a number of essential noncanonical functions including regulation of metabolic homeostasis, cell proliferation and differentiation, angiogenesis, tumorigenesis, and immune response.[1,2]

Currently, treatment options for FARS1 patients are limited to symptomatic treatment. In some patients (P2, P7; Figure 4) pulmonary alveolar proteinosis, that is, excessive accumulation of lipoproteins in the alveolar space, characterizes their interstitial lung disease in addition to cholesterol pneumonitis. Whole lung lavage treatment achieved transient relief of respiratory insufficiency in those two subjects treated with this option (Figure 3(K)). Increasing the substrate, that is, the metabolic concentration

FIGURE 5 FARS1 structure, localization of mutations, protein expression level, and enzymatic activity. (A) Schematic of FARSA protein with location of missense mutations in the catalytic domain A1/2 (*case report[10]) (B) Location of mutations in the structural model of FARS1 complexed with tRNA^Phe in cartoon backbone representation. Two FARSA chains are colored in light gray and green, two FARSB chains in dark gray and blue, tRNA^Phe in orange. Mutated amino acid residues are shown in black. (C) Predicted impact of mutations on local amino acid interactions with pairwise comparison between side chains of wildtype residues (left) and modeled missense mutations (right). Mutated residues are shown in black, the phenylalanyl-adenylate in yellow. Colors blue, red, and yellow highlight single nitrogen, oxygen, and sulfur atoms. (D) Representative Western blots of FARSA and FARSB protein expression in cells of patients and relatives. (E) FARS1 aminoacylation activity in cytosolic cell fractions of patients and relatives. Data represent mean ± SD of at least three technical replicates. P3 fibroblasts were unavailable. DBD, DNA/dsRNA-binding domain [Colour figure can be viewed at wileyonlinelibrary.com]

of the synthetase's respective amino acid, here phenylalanine, appears to be a safe therapeutic option which can be instituted in individual patients, but needs to be addressed in clinical trials. Anecdotal evidence supports this approach for patients with interstitial lung–liver disease due to mutations in MARS1.[27]

Novel therapeutic options are expected with a deeper understanding of FARS1-linked recessive disease. Its association with a broad and variable spectrum of symptoms calls for alertness in clinical practice. Genetic screening for mutations in *FARSA* and *FARSB* may help guide diagnostics and should be considered for unclear cases of multisystem disorders in combination with chronic interstitial lung disease.

CONFLICT OF INTEREST

The authors declare no conflicts of interest.

PEER REVIEW

The peer review history for this article is available at https://publons.com/publon/10.1111/cge.13943.

DATA AVAILABILITY STATEMENT

The data that support the findings of this study are available from the corresponding author, Matthias Griese, upon reasonable request.

ORCID

Luise A. Schuch https://orcid.org/0000-0002-7445-4895
Maria Forstner https://orcid.org/0000-0002-1468-6969
Christina K. Rapp https://orcid.org/0000-0002-7371-8158
Yang Li https://orcid.org/0000-0001-8123-0876
Desiree E. C. Smith https://orcid.org/0000-0003-2053-3392
Marisa I. Mendes https://orcid.org/0000-0002-6617-3698
Florent Delhommel https://orcid.org/0000-0001-7021-087X
Michael Sattler https://orcid.org/0000-0002-1594-0527
Nagehan Emiralioğlu https://orcid.org/0000-0002-1405-8401
Ekim Z. Taskiran https://orcid.org/0000-0001-6040-6625
Diclehan Orhan https://orcid.org/0000-0003-3637-5392
Nural Kiper https://orcid.org/0000-0003-1261-7393
Tim Jeske https://orcid.org/0000-0003-2511-4699
Maximilian Hastreiter https://orcid.org/0000-0003-3288-4229
Alba Torrent-Vernetta https://orcid.org/0000-0002-3575-2427
Antonio Moreno-Galdó https://orcid.org/0000-0002-2496-9786
Matthias Griese https://orcid.org/0000-0003-0113-912X

REFERENCES

1. Guo M, Yang XL, Schimmel P. New functions of aminoacyl-tRNA synthetases beyond translation. *Nat Rev Mol Cell Biol*. 2010;11:668-674. https://doi.org/10.1038/nrm2956.
2. Paul M, Schimmel P. Essential nontranslational functions of tRNA synthetases. *Nat Chem Biol*. 2013;9:145-153. https://doi.org/10.1038/nchembio.1158.
3. Sissler M, González-Serrano LE, Westhof E. Recent advances in mitochondrial aminoacyl-tRNA synthetases and disease. *Trends Mol Med*. 2017;23:693-708. https://doi.org/10.1016/j.molmed.2017.06.002.
4. Fuchs SA, Schene IF, Kok G, et al. Aminoacyl-tRNA synthetase deficiencies in search of common themes. *Genet Med*. 2019;21:319-330. https://doi.org/10.1038/s41436-018-0048-y.
5. Meyer-Schuman R, Antonellis A. Emerging mechanisms of aminoacyl-tRNA synthetase mutations in recessive and dominant human disease. *Hum Mol Genet*. 2017;26:R114-R127. https://doi.org/10.1093/hmg/ddx231.
6. Kuo ME, Theil AF, Kievit A, et al. Cysteinyl-tRNA synthetase mutations cause a multi-system, recessive disease that includes microcephaly, developmental delay, and brittle hair and nails. *Am J Hum Genet*. 2019;104(3):520–529. https://doi.org/10.1016/j.ajhg.2019.01.006.
7. Mendes MI, Gutierrez Salazar M, Guerrero K, et al. Bi-allelic mutations in EPRS, encoding the glutamyl-prolyl-aminoacyl-tRNA synthetase, cause a hypomyelinating leukodystrophy. *Am J Hum Genet*. 2018;102(4):676-684. https://doi.org/10.1016/j.ajhg.2018.02.011.
8. Theil AF, Botta E, Raams A, et al. Bi-allelic TARS mutations are associated with brittle hair phenotype. *Am J Hum Genet*. 2019. 105(2):434-440https://doi.org/10.1016/j.ajhg.2019.06.017.
9. Xu Z, Lo WS, Beck DB, et al. Bi-allelic mutations in Phe-tRNA synthetase associated with a multi-system pulmonary disease support nontranslational function. *Am J Hum Genet*. 2018;103(1):100–114. https://doi.org/10.1016/j.ajhg.2018.06.006.
10. Krenke K, Szczałuba K, Bielecka T, et al. FARSA mutations mimic phenylalanyl-tRNA synthetase deficiency caused by FARSB defects. *Clin Genet*. 2019;96:468-472. https://doi.org/10.1111/cge.13614.
11. Safro M, Moor N, Lavrik O. Phenylalanyl-tRNA synthetase. In M. Ibba, C.S. Francklyn, S. Cusack (Eds.), *The Aminoacyl-tRNA Synthetases*. George Town, TX: Landes Bioscience (2004). 2000;250–265.
12. Zadjali F, Al-Yahyaee A, Al-Nabhani M, et al. Homozygosity for FARSB mutation leads to Phe-tRNA synthetase-related disease of growth restriction, brain calcification, and interstitial lung disease. *Hum Mutat*. 2018;39:1355-1359. https://doi.org/10.1002/humu.23595.
13. Antonellis A, Oprescu SN, Griffin LB, Heider A, Amalfitano A, Innis JW. Compound heterozygosity for loss-of-function FARSB variants in a patient with classic features of recessive aminoacyl-tRNA synthetase-related disease. *Hum Mutat*. 2018;39:834-840. https://doi.org/10.1002/humu.23424.
14. Li H, Durbin R. Fast and accurate long-read alignment with burrows-wheeler transform. *Bioinformatics*. 2010;26:589-595. https://doi.org/10.1093/bioinformatics/btp698.

15. McKenna A, Hanna M, Banks E, et al. The genome analysis toolkit: a MapReduce framework for analyzing next-generation DNA sequencing data. *Genome Res*. 2010;20(9):1297-1303. https://doi.org/10.1101/gr.107524.110.

16. McLaren W, Pritchard B, Rios D, Chen Y, Flicek P, Cunningham F. Deriving the consequences of genomic variants with the Ensembl API and SNP effect predictor. *Bioinformatics*. 2010;26:2069-2070. https://doi.org/10.1093/bioinformatics/btq330.

17. Auton A, Abecasis GR, Altshuler DM, et al. A global reference for human genetic variation. *Nature*. 2015;526:68-74. https://doi.org/10.1038/nature15393.

18. Karczewski KJ, Francioli LC, Tiao G, et al. The mutational constraint spectrum quantified from variation in 141,456 humans. *Nature*. 2020;581(7809):434–443. http://dx.doi.org/10.1038/s41586-020-2308-7.

19. Hager P, Mewes HW, Rohlfs M, Klein C, Jeske T. SmartPhase: accurate and fast phasing of heterozygous variant pairs for genetic diagnosis of rare diseases. *PLoS Comput Biol*. 2020;16:7613. https://doi.org/10.1371/journal.pcbi.1007613.

20. Moor N, Kotik-Kogan O, Tworowski D, Sukhanova M, Safro M. The crystal structure of the ternary complex of phenylalanyl-tRNA synthetase with tRNAPhe and a phenylalanyl-adenylate analogue reveals a conformational switch of the CCA end. *Biochemistry*. 2006;45:10572-10583. https://doi.org/10.1021/bi060491l.

21. Finarov I, Moor N, Kessler N, Klipcan L, Safro MG. Structure of human cytosolic phenylalanyl-tRNA synthetase: evidence for kingdom-specific design of the active sites and tRNA binding patterns. *Structure*. 2010;18:343-353. https://doi.org/10.1016/j.str.2010.01.002.

22. Schrödinger L. The PyMol Molecular Graphics System, Versión 1.8. Thomas Hold. 2015. https://doi.org/10.1007/s13398-014-0173-7.2

23. Ashkenazy H, Abadi S, Martz E, et al. ConSurf 2016: an improved methodology to estimate and visualize evolutionary conservation in macromolecules. *Nucleic Acids Res*. 2016;44:344-350. https://doi.org/10.1093/nar/gkw408.

24. Schmittgen TD, Livak KJ. Analyzing real-time PCR data by the comparative CT method. *Nat Protoc*. 2008;3(6):1101-1108. https://doi.org/10.1038/nprot.2008.73.

25. Schindelin J, Arganda-Carreras I, Frise E, et al. Fiji: an open-source platform for biological-image analysis. *Nat Methods*. 2012;9:676-682. https://doi.org/10.1038/nmeth.2019.

26. Klipcan L, Finarov I, Moor N, Safro MG. Structural aspects of phenylalanylation and quality control in three major forms of phenylalanyl-tRNA synthetase. *J Amino Acids*. 2010;2010:1-7. https://doi.org/10.4061/2010/983503.

27. Lenz D, Stahl M, Seidl E, et al. Rescue of respiratory failure in pulmonary alveolar proteinosis due to pathogenic MARS1 variants. *Pediatr Pulmonol*. 2020;55:3057-3066. https://doi.org/10.1002/ppul.25031.

SUPPORTING INFORMATION

Additional supporting information may be found online in the Supporting Information section at the end of this article.